Commun. Comput. Phys.
doi: 10.4208/cicp.270513.130314a

Vol. **16**, No. 3, pp. 675-698
September 2014

Direct Numerical Simulation of Multiple Particles Sedimentation at an Intermediate Reynolds Number

Deming Nie[1], Jianzhong Lin[1,2,*] and Mengjiao Zheng[1]

[1] *Institute of Fluid Mechanics, China Jiliang University, Hangzhou, 310018, China.*
[2] *State Key Laboratory of Fluid Power Transmission and Control, Zhejiang University, Hangzhou 310027, China.*

Received 27 May 2013; Accepted (in revised version) 13 March 2014

Communicated by Boo-Cheong Khoo

Available online 24 June 2014

Abstract. In this work the previously developed Lattice Boltzmann-Direct Forcing/ Fictitious Domain (LB-DF/FD) method is adopted to simulate the sedimentation of eight circular particles under gravity at an intermediate Reynolds number of about 248. The particle clustering and the resulting Drafting-Kissing-Tumbling (DKT) motion which takes place for the first time are explored. The effects of initial particle-particle gap on the DKT motion are found significant. In addition, the trajectories of particles are presented under different initial particle-particle gaps, which display totally three kinds of falling patterns provided that no DKT motion takes place, i.e. the concave-down shape, the shape of letter "M" and "in-line" shape. Furthermore, the lateral and vertical hydrodynamic forces on the particles are investigated. It has been found that the value of Strouhal number for all particles is the same which is about 0.157 when initial particle-particle gap is relatively large. The wall effects on falling patterns and particle expansions are examined in the final.

AMS subject classifications: 76T20, 76-02, 76M28

PACS: 47.11.-j, 47.57.ef, 47.57.E-, 47.55.-t

Key words: Lattice Boltzmann method, sedimentation, fictitious domain, falling pattern.

1 Introduction

Solid particles immersed in a viscous fluid lead to a two-phase flow problem, which is very common in nature and many industrial processes, including atmospheric currents,

*Corresponding author. *Email addresses:* nieinhz@cjlu.edu.cn (D. Nie), mecjzlin@public.zju.edu.cn (J. Lin), dreambanana@163.com (M. Zheng)

aerosol deposition, pharmaceutical sciences, hydraulic fracturing, fluidized beds and so on. It is important to understand particle-particle interactions and particle-fluid interactions, and their microstructure evolution in fluids, which usually relates to the collective behaviour and self-organization of solid particles, and is central to physical phenomena such as cloud formation, particle suspension and particle sedimentation. In comparison with experimental measurements, numerical simulations have remarkable advantages in exploring the inter-phase interactions in multiphase flows, especially for direct numerical simulation (DNS) methods. In a DNS method, the fluid flow and particle motion are coupled to study the dynamics of individual particles suspended in fluids, which is the highest-resolution numerical method without any empirical model.

So far extensive theoretical and numerical models (Hocking, 1964; Crowley, 1971; Leichtberg et al., 1976; Brady and Bossis, 1988; Mo and Sangani, 1994; Feng and Joseph, 1995; Alexander et al., 2003; Nguyen and Ladd, 2005; Metzger et al., 2007; Koch and Subramanian, 2011) have been proposed to simulate the dynamics of many interacting particles in a viscous fluid at quasi-steady zero-Reynolds-number or low Reynolds number by ignoring the transient and nonlinear inertia effects, which are becoming crucial at intermediate Reynolds numbers or high Reynolds numbers. The hydrodynamic interactions between particles mediated by the fluid and particle interactions with the wall are highly nonlinear and the dynamics of multiple particles can be quite complex by taking into account the fluid inertia, which also introduces unsteadiness to particulate flow problems. In comparison with the numerical studies at low Reynolds numbers, much fewer studies have been found on particle interactions and clustering at intermediate Reynolds numbers due to the difficulty in dealing with the boundaries between particles and fluid in a DNS framework. Jenny et al. (2004) numerically investigated a sphere falling or ascending under the action of gravity in a Newtonian fluid at intermediate Reynolds numbers. Their results show that the sphere undergoes a transition to a full spatio-temporal chaos in the range of asymptotic average Reynolds number lying between 205 and 310, and the scenario is significantly different for falling and for ascending spheres (Jenny et al., 2004). Recently, Yacoubi et al. (2012) presented remarkable work by studying the two-dimensional dynamics of horizontal arrays of settling cylinders in a container at intermediate Reynolds numbers of 200 based on the immersed interface method. They found that in the case of odd-numbered arrays, the middle cylinder is always leading, whereas in the case of even-numbered arrays, the steady-state shape is concave-down. Furthermore, in large arrays (the number of particles greater than 5) the outer pairs tend to cluster. However, they did not further investigate the influence of initial particle-particle gaps on falling patterns, especially for small or large initial gaps, which is expected to be central to particle clustering and also to the resulting well-known 'Drafting-Kissing-Tumbling (DKT)' motion. Furthermore, it is helpful to better understand the dynamics of interacting particles moving freely under the action of gravity, buoyancy and hydrodynamic forces by studying the lateral and longitudinal expansions of the array. In addition, it is also necessary to examine the wall effects, i.e. the effects of the width of container on the dynamics of particle clustering. The present work is mostly

motivated by these reasons.

The lattice Boltzmann method (LBM) has proved to be a powerful numerical scheme for the simulation of particle suspensions, multiphase flow, microfluidics, and turbulence due to its several remarkable advantages since it was originated. Application of LBM to simulate particles suspended in a viscous fluid was first proposed by Ladd (1994) and then improved by Aidun et al. (1998). In their applications, the non-slip condition on the particle-fluid interface is treated by the bounce-back rule and the particle surface is represented by the boundary nodes, which are essentially a set of the mid-points of the links between two fixed grids. In order to better deal with fluid-solid interface problems, Feng and Michaelides (2004) incorporated the immersed boundary method (IBM) into LBM for two-dimensional and three-dimensional fluid-particle systems, which is known as IB-LBM. Similarly, Tian et al. (2011) successfully developed another immersed boundary-lattice Boltzmann method for hydrodynamic interaction of deformable bodies. Nie and Lin (2010) proposed a single-relaxation-time (SRT) based lattice Boltzmann-Direct Forcing/Fictitious Domain (LB-DF/FD) method for the simulation of particle suspensions, which was derived from SRT-LBM coupled with direct-forcing/fictitious domain (DF/FD) method (Yu and Shao, 2007). It has been shown that the LB-DF/FD method is capable of dealing with spherical particle motion (Nie and Lin, 2011a) and non-spherical particle motion (Nie et al., 2011; Nie and Lin, 2011b), which is also suitable to simulate particle sedimentation in the intermediate Reynolds number regime (Nie et al., 2012).

The main objective of this study is to numerically investigate the dynamics and interactions of eight circular particles settling in a vertical container at a Reynolds number of about 248 by the LB-DF/FD method. Firstly, the previously developed LB-DF/FD method is updated by introducing the multiple-relaxation-time (MRT) model, instead of the SRT model. The MRT model is the most general form derived from the linearized collision model within the theoretical framework of the LB equations and kinetic theory — it includes all possible degrees of freedom to optimize the LB equations (Luo et al. 2011). The validation of the MRT based LB-DF/FD method is presented in Section 3.1. Secondly, this method is adopted to simulate eight particles falling in a Newtonian fluid under gravity. The width of computational domain, i.e. the container with is relatively large in the simulations, which is at least 50 times particle diameter. First of all the focus attention would be on the DKT motion which takes place for the first time in the falling process. Results show that the particle clustering depends on the initial particle-particle gap. The observation that the outermost particles tend to cluster, which was made by Yacoubi et al. (2012), is only one of possible situations. Then the focus moves to the trajectories of particles which displays different falling patterns provided that particle collisions do not occur when the initial gap varies. The detailed description is presented in Section 3.2. The lateral and vertical expansions of the particles which are expressed by their own variances are quantitatively presented in the following section. The lateral and vertical hydrodynamic forces on the particles are investigated by introducing their corresponding force coefficients in Section 3.4. In Section 3.5 the wall effects on the trajec-

tories of particles and the lateral and longitudinal expansions are assessed. A summary is presented in Section 4.

2 Numerical detail

2.1 Multiple-relaxation-time model

In LB-DF/FD method, the lattice Boltzmann equations are solved for the fluid flow and the fictitious domain scheme is used to solve fluid-solid interactions. The lattice Boltzmann method is based on the SRT model, which is also known as the Bhatnagar-Gross-Krook (BGK) model (Qian et al., 1992). In this work, the MRT model is introducing which is shown to be superior over the SRT model (Nie and Lin, 2010). The discrete MRT lattice Boltzmann equations under external forces are described as,

$$f_i(\boldsymbol{x}+\boldsymbol{e}_i\Delta t,t+\Delta t)-f_i(\boldsymbol{x},t)=-M^{-1}S\left[\boldsymbol{m}-\boldsymbol{m}^{(eq)}\right]+\boldsymbol{F}\Delta t, \tag{2.1}$$

where S is the collision matrix which is diagonal. Through the transform matrix M, the velocity space spanned by f_i and the moment space spanned by m_i are related by a linear mapping: $\boldsymbol{m}=M\cdot\boldsymbol{f}$, $\boldsymbol{f}=M^{-1}\cdot\boldsymbol{m}$. In this work we adopt the D2Q9 lattice model, of which the discrete velocity set is,

$$c_i=\begin{cases}(0,0), & i=0,\\ (\pm1,0)c,(0,\pm1)c, & i=1-4,\\ (\pm1,\pm1)c,(\pm1,\pm1)c, & i=5-8,\end{cases}$$

where $c=\Delta x/\Delta t$, Δx is the lattice spacing and Δt is the time step. The speed of sound c_s is determined by,

$$c_s=\frac{1}{\sqrt{3}}c.$$

Corresponding to the D2Q9 model, the moments are given (Luo et al., 2011) by $m_0=\rho$, $m_1=e$, $m_2=\varepsilon$, $m_3=j_x$, $m_4=q_x$, $m_5=j_y$, $m_6=q_y$, $m_7=p_{xx}$ and $m_8=p_{xy}$, among which the density ρ and the flow momentum $\boldsymbol{j}=(j_x,j_y)=\rho\boldsymbol{u}$ are the conserved moments in the system. The diagonal matrix of non-negative relaxation rates $0<s_i<2$ is given by $S=\mathrm{diag}(0,s_e,s_\varepsilon,0,s_q,0,s_q,s_\nu,s_\nu)$, and $s_\nu=1/\tau$, and τ is a non-dimensional relaxation time associated with the fluid shear viscosity. If all the relaxation rates is equal to $1/\tau$, then the MRT model reduces to the LBGK or SRT model. According to Luo et al. (2011), the equilibria of the non-conserved moments are given below,

$$e^{(eq)}=-2\rho+\frac{3\boldsymbol{j}\cdot\boldsymbol{j}}{\rho},\qquad \varepsilon^{(eq)}=\rho-\frac{3\boldsymbol{j}\cdot\boldsymbol{j}}{\rho},\qquad \left({q_x}^{(eq)},{q_y}^{(eq)}\right)=-\left(j_x,j_y\right), \tag{2.2a}$$

$${p_{xx}}^{(eq)}=\frac{\left({j_x}^2-{j_y}^2\right)}{\rho},\qquad {p_{xy}}^{(eq)}=\frac{j_xj_y}{\rho}. \tag{2.2b}$$

With the discrete velocities of D2Q9 and the moments given above, the transformation matrix M is determined by (Luo et al., 2011),

$$M=\begin{bmatrix} 1 & 1 & 1 & 1 & 1 & 1 & 1 & 1 & 1 \\ -4 & -1 & -1 & -1 & -1 & 2 & 2 & 2 & 2 \\ 4 & -2 & -2 & -2 & -2 & 1 & 1 & 1 & 1 \\ 0 & 1 & 0 & -1 & 0 & 1 & -1 & -1 & 1 \\ 0 & -2 & 0 & 2 & 0 & 1 & -1 & -1 & 1 \\ 0 & 0 & 1 & 0 & -1 & 1 & 1 & -1 & 1 \\ 0 & 0 & -2 & 0 & 2 & 1 & 1 & -1 & -1 \\ 0 & 1 & -1 & 1 & -1 & 0 & 0 & 0 & 0 \\ 0 & 0 & 0 & 0 & 0 & 1 & -1 & 1 & -1 \end{bmatrix}. \tag{2.3}$$

Guo et al. (Guo et al., 2002) presented a method to include the body force into the LBM, in which the discrete lattice effect and the contributions of the body force to the momentum flux are both considered, leading to the exact Navier-Stokes equations. In this work we also adopt the proposed method (Guo et al., 2002). In Eq. (2.1), the forcing term $\boldsymbol{F}$ is defined by,

$$\boldsymbol{F}=M^{-1}\left(I-\frac{1}{2}S\right)M\overline{\boldsymbol{F}},\qquad \overline{F_i}=w_i\left[\frac{\boldsymbol{c}_i\cdot\boldsymbol{\lambda}}{c_s^2}+\frac{\boldsymbol{u\lambda}:\boldsymbol{c}_i\boldsymbol{c}_i}{c_s^4}-\frac{\boldsymbol{u\lambda}:c_s^2\boldsymbol{I}}{c_s^4}\right], \tag{2.4}$$

where $\boldsymbol{\lambda}$ is a pseudo body force which is introduced to enforce the (fictitious) fluids to satisfy the constraint of rigid body motion in the fictitious domain scheme (Nie and Lin, 2011a). w_i are weights related to the lattice model which are chosen as the following values: $w_0=4/9$; $w_i=1/9$, $i=1\sim4$; $w_i=1/36$, $i=5\sim8$.

By applying the Chapman-Enskog analysis and Taylor expansion techniques, Eq. (2.1) leads to the following hydrodynamic equations,

$$\nabla\cdot\boldsymbol{u}=0, \tag{2.5a}$$

$$\rho_f\left(\frac{\partial\boldsymbol{u}}{\partial t}+(\boldsymbol{u}\cdot\nabla)\boldsymbol{u}\right)=-\nabla p+\mu\nabla^2\boldsymbol{u}+\boldsymbol{\lambda}. \tag{2.5b}$$

The shear viscosity ν and the bulk viscosity ζ are,

$$\nu=\frac{1}{3}\left(\frac{1}{s_\nu}-\frac{1}{2}\right)c\Delta x,\qquad \zeta=\frac{1}{3}\left(\frac{1}{s_e}-\frac{1}{2}\right)c\Delta x. \tag{2.6}$$

2.2 LB-DF/FD method

The LB-DF/FD method is briefly explained in this section since those are explained in detail elsewhere (Nie and Lin, 2010).

In DF/FD method, the interior domains of the particles are filled with the same fluids as the surroundings and a pseudo body force λ is introduced to enforce the interior

(fictitious) fluids to satisfy the constraint of rigid body motion, as described by,

$$\boldsymbol{u}=\boldsymbol{U}+\boldsymbol{\omega}_s\times\boldsymbol{r} \qquad \text{(the particle inner domain, } P\text{)}, \tag{2.7}$$

where $\boldsymbol{U}$ and $\boldsymbol{\omega}_s$ are the particle translational velocity and angular velocity, respectively, and $\boldsymbol{r}$ is the position vector with respect to the particle mass center. Moreover, in DF/FD method, a certain number of Lagrangian nodes are distributed to represent the particle in the simulations, which is shown in the following (Fig. 2).

The particle motion with mass M_p and moment of inertia J_p is governed by Newton's equations,

$$M_p\frac{d\boldsymbol{U}}{dt}=\boldsymbol{F}_H+\left(1-\frac{1}{\rho_r}\right)M_p\boldsymbol{g}+\boldsymbol{F}_C, \tag{2.8}$$

$$J_p\frac{d\boldsymbol{\omega}_s}{dt}=\boldsymbol{T}_H, \tag{2.9}$$

where $\boldsymbol{F}_H$ and $\boldsymbol{T}_H$ are the hydrodynamic forces and torques on the particle, respectively, defined as,

$$\boldsymbol{F}_C=\int_{\partial P}\boldsymbol{n}\cdot\sigma ds, \tag{2.10a}$$

$$\boldsymbol{T}_C=\int_{\partial P}\boldsymbol{r}\times(\boldsymbol{n}\cdot\sigma)ds, \tag{2.10b}$$

where σ is the fluid stress tensor, $\boldsymbol{n}$ is the unit outward normal on the particle surface. $\boldsymbol{F}_C$ denotes particle-particle and particle-wall collision forces. $\boldsymbol{g}$ is the gravitational acceleration, and ρ_r is the solid-fluid density ratio, i.e., $\rho_r=\rho_p/\rho_f$.

Based on a direct-forcing scheme, the forcing term exerted on the Lagrangian points in the particle domain can be expressed as,

$$\lambda^{n+1}=\rho_f\frac{\boldsymbol{u}^{n+1}-\boldsymbol{u}^*}{\Delta t}=\rho_f\frac{\boldsymbol{U}^{n+1}+{\boldsymbol{\omega}_s}^{n+1}\times\boldsymbol{r}-\boldsymbol{u}^*}{\Delta t}, \tag{2.11}$$

where $\boldsymbol{u}^*$ is a temporary velocity which satisfies the momentum equation (2.5b) with zero body-force.

From (2.7)-(2.11), one can obtain the equations for updating particle motion,

$$M_p\frac{\boldsymbol{U}^{n+1}}{\Delta t}=M_p\left(1-\frac{1}{\rho_r}\right)\frac{\boldsymbol{U}^n}{\Delta t}+\left(1-\frac{1}{\rho_r}\right)M_p\boldsymbol{g}+\int_P\rho_f\frac{\boldsymbol{u}^*}{\Delta t}d\Omega+\boldsymbol{F}_C^{n+1}, \tag{2.12}$$

$$J_p\frac{{\boldsymbol{\omega}_s}^{n+1}}{\Delta t}=J_p\left(1-\frac{1}{\rho_r}\right)\frac{{\boldsymbol{\omega}_s}^n}{\Delta t}+\int_P\rho_f\boldsymbol{r}\times\frac{\boldsymbol{u}^*}{\Delta t}d\Omega. \tag{2.13}$$

As shown from (2.12) and (2.13), the hydrodynamic forces and torques exerted on the particle do not appear explicitly. As a result it's unnecessary to calculate them to update the particle motion.

The whole problem is decoupled into the fluid and solid particle sub-problems with the fractional step scheme, which includes the following steps:

(i) Calculate $f^*(\boldsymbol{x},t)$ from Eq. (2.1) without the body force and then $\boldsymbol{u}^*$ is obtained.

(ii) Based on Eq. (2.12) and (2.13), calculate translational velocity $\boldsymbol{U}$ and angular velocity $\boldsymbol{\omega}_s$.

(iii) Update pseudo body-force λ^{n+1} inside the particle domain through Eq. (2.11).

(iv) Introduce body-force λ^{n+1} into Eq. (2.1) and calculate $f(\boldsymbol{x},t)$ without collision, then the new ρ_f and $\boldsymbol{u}$ determined.

2.3 Short-range repulsive force

In order to prevent particles overlapping, a model for particle-particle interactions is needed in the simulations. The short range repulsive force proposed by Wan and Turek (Wan and Turek, 2007) is adopted in this work, which is easily carried out in the code. For particle-particle interactions, the repulsive force is determined as,

$$\boldsymbol{F}_{i,j}^{P}=\begin{cases}0, & d_{i,j}>R_i+R_j+\xi,\\ \frac{1}{\varepsilon_p'}\left(\boldsymbol{X}_i-\boldsymbol{X}_j\right)\left(R_i+R_j-d_{i,j}\right), & d_{i,j}\leqslant R_i+R_j,\\ \frac{1}{\varepsilon_p}\left(\boldsymbol{X}_i-\boldsymbol{X}_j\right)\left(R_i+R_j+\xi-d_{i,j}\right)^2, & R_i+R_j\leqslant d_{i,j}\leqslant R_i+R_j+\xi,\end{cases} \tag{2.14}$$

where R_i and R_j are the radius of the ith and jth particle, $\boldsymbol{X}_i$ and $\boldsymbol{X}_j$ are the coordinates of their mass centers, $d_{i,j}=|\boldsymbol{X}_i-\boldsymbol{X}_j|$ is the distance between their mass centers, ξ is the force range which is usually set to be one or two lattice spacing. ε_p' and ε_p are two small positive stiffness parameters for particle-particle collisions. For the particle-wall interactions, the corresponding repulsive force is determined as,

$$\boldsymbol{F}_{i,j}^{W}=\begin{cases}0, & d_i'>2R_i+\xi,\\ \frac{1}{\varepsilon_\omega'}\left(\boldsymbol{X}_i-\boldsymbol{X}_i'\right)\left(2R_i-d_i'\right), & d_i'\leqslant 2R_i,\\ \frac{1}{\varepsilon_\omega}\left(\boldsymbol{X}_i-\boldsymbol{X}_i'\right)\left(2R_i+\xi-d_i'\right)^2, & 2R_i\leqslant d_i'\leqslant 2R_i+\xi,\end{cases} \tag{2.15}$$

where X_i' is the coordinate vector of the center of the nearest imaginary particle located on the boundary and $d_i'=|X_i-X_i'|$. ε_w' and ε_w are another two small positive stiffness parameters for particle-wall collisions.

2.4 Problem description

A schematic diagram of the physical model is shown in Fig. 1. Eight circular particles in a horizontal arrangement with zero initial velocity are released in a vertical container. In order to better visualize numerical results, four kinds of color are used to distinguish among the particles, i.e. red, dark blue, purple, light blue, from the middle to the outside. For convenience of description, the particles are named from Particle 1 to Particle 8 in sequence, from left to right. D is the particle diameter and h_0 is the initial particle-particle gap which is the closest distance between two neighboring particles. The grid size is fixed

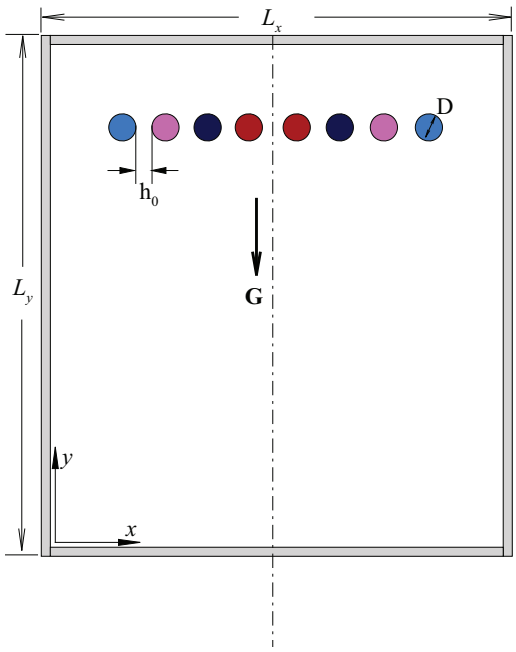

Figure 1: A schematic diagram of the physical model.

at $\Delta x=1/48D$ and the container height is fixed at $L_y=100D$. In physical units, the density of the fluid and the particle are taken to be $\rho_f=1.0\text{g/cm}^3$ and $\rho_p=1.5\text{g/cm}^3$, respectively, the diameter of the particle D is 0.2cm and the kinematic viscosity of the fluid ν is set to be 0.01 $\text{cm}^2\ \text{s}^{-1}$. The velocity scale in the simulations is given by,

$$U=\sqrt{\frac{\pi D(\rho_r-1)g}{2}}. \tag{2.16}$$

The time scale is expressed by $T=D/U$. Therefore, the Reynolds number defined by $Re=UD/\nu$ is about 248 in the present simulations. In order to reduce the impact of the container walls on flow pattern as much as possible, the container width is chosen large enough in this work, which is depending on the initial inter-particle gap, as shown in Table 1. The non-dimensional parameters h_0' and L_x' are defined by $h_0'=h_0/D$ and $L_x'=L_x/D$. The impact of the container width will be investigated in this work. For convenience no-slip boundary conditions are set on all four fixed walls of the domain. This avoids specifying the far-field boundary conditions on a finite computational domain.

Table 1: The container width L_x' for different initial particles gap h_0'.

h_0'	≤ 0.7	≤ 1.2	1.5	2.0	3.0	4.0	5.0
L_x'	50	60	80	80	80	80	80

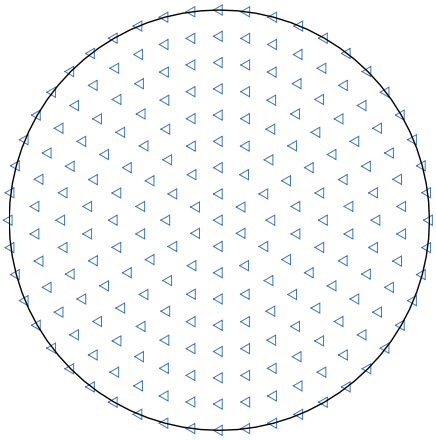

Figure 2: Arrangements of Lagrangian points for circular particle.

The arrangement of Lagrangian points inside the circular particle is shown in Fig. 2, one point at the particle center, and $6i$ points on the ith ring.

3 Numerical results

3.1 Validation

First of all the benchmark problem of flow over a fixed circular cylinder at $Re=100$ and 200 is adopted to validate the present method. The lattice spacing is $\Delta x=1/40D$. Table 2 presents the mean value and amplitude of drag and lift coefficients and Strouhal number of present SRT and MRT results as well as numerical results of previous researchers. On one hand it is observed that both of SRT and MRT results agree reasonably well with those reported by other researchers. On the other hand, Fig. 3 shows the instantaneous pressure distribution close to the cylinder. As shown in the figure, the general features of the pressure obtained by the MRT and SRT model are similar, while severe oscillations

Table 2: Comparison of flow parameter values for flow past single circular cylinder at $Re=100$ and 200.

	$Re=100$				$Re=200$		
	C_D	C_L	St		C_D	C_L	St
Uhlmann (2005)	1.453±0.011	±0.339	0.169	Braza et al. (1986)	1.40±0.050	±0.75	0.200
Xu and Wang (2006)	1.423±0.013	±0.340	0.171	Mark et al. (2005)	1.37±0.046	±0.70	0.199
Ding et al. (2007)	1.356±0.010	±0.287	0.166	Ding et al. (2007)	1.348±0.050	±0.659	0.196
Xu (2008)	1.42±0.010	±0.353	0.172	Xu (2008)	1.43±0.050	±0.71	0.202
Present SRT	1.406±0.011	±0.364	0.165	Present SRT	1.419±0.052	±0.751	0.195
Present MRT	1.398±0.011	±0.359	0.165	Present MRT	1.414±0.052	±0.745	0.196

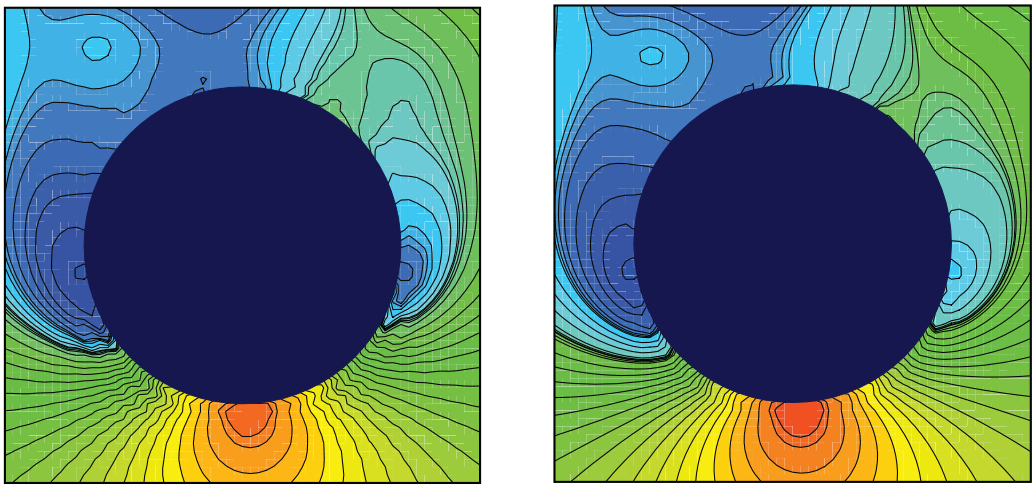

(a) SRT result (b) MRT result

Figure 3: Instantaneous pressure distribution close to the cylinder at $Re=200$.

close to the cylinder are observed in the pressure obtained by using the SRT model, in contrast to the much smoother result obtained by using the MRT model, which states that the MRT model has better ability of computing pressure than the SRT model. This is consistent with the work done by Luo et al. (2011) and Nie et al. (2013). In addition, it's worth stating that if a coarser grid is adopted, i.e. if $\Delta x<1/40D$, more severe oscillations throughout the entire computational domain are expected to be observed in the pressure field for the SRT model.

3.2 Falling pattern

Fig. 4 shows the instantaneous vorticity contours for initial gap $h_0'=0.1$ at different times, which is the smallest value of h_0' that was simulated. It's noticeable that they are all bilateral symmetrical about the centerline. As time evolves the four particles (dark blue and red) in the middle tend to cluster and form two pairs (Particle 3 and Particle 4, Particle 5 and Particle 6), as shown in Figs. 4(c) and (d). After a while the left pair begins to tumble clockwise. Similarly, the right pair tumbles counter-clockwise, as shown in Figs. 4(e) and (f). The particles do not come into contact and their dynamics are reminiscent of the well-known 'Drafting-Kissing-Tumbling (DKT)' motion. The name of DKT comes about since the trailing particle drifts in the wake of the leading one to begin with, rapidly approaching it from behind, and the pair eventually tumbles with subsequent increase in the transverse separation. The DKT pair interactions lead to a rapid local rearrangement in particle positions, which is obvious in Fig. 4. Furthermore, as shown in Figs. 4(g)-(h), the two outermost particles also tend to cluster and reproduce the DKT motion. The leftmost pair (Particle 1 and Particle 2) tumbles clockwise and the rightmost pair (Parti-

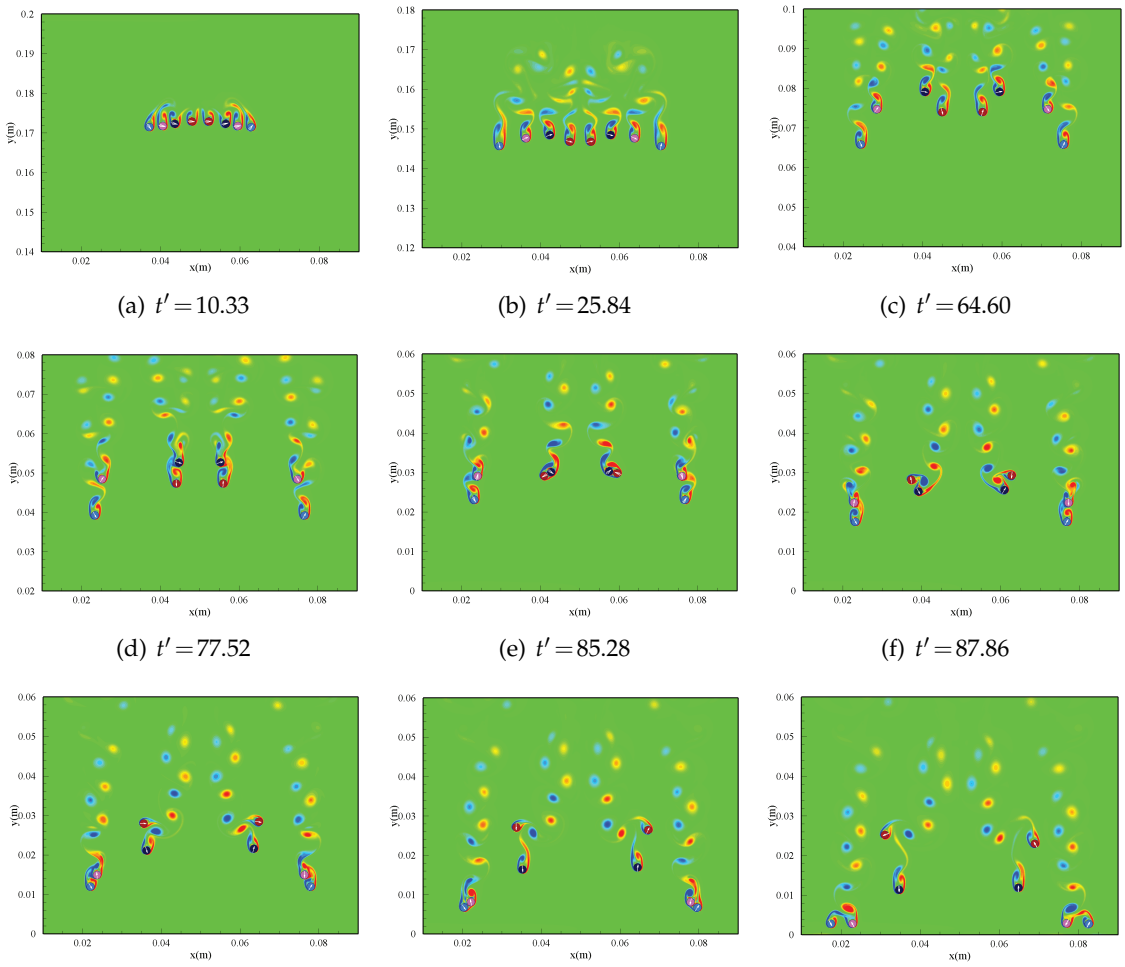

(a) $t'=10.33$ (b) $t'=25.84$ (c) $t'=64.60$

(d) $t'=77.52$ (e) $t'=85.28$ (f) $t'=87.86$

(g) $t'=90.45$ (h) $t'=93.03$ (i) $t'=95.61$

Figure 4: Instantaneous vorticity contour for $h_0'=0.1$.

cle 7 and Particle 8) tumbles counter-clockwise. It should be pointed out that the DKT motion usually takes place more than once for small initial gap h_0, which is the key mechanism of arranging particle positions in the sedimentation, as shown in our simulations. However, the short range repulsive force model adopted in this work is a hypothetical collision model to prevent particles overlapping. As matter of fact, the DKT motion is sensitive to the repulsive force. Therefore, in this work much attention is paid to the DKT motion which takes place for the first time in the sedimentation.

The first DKT motion in the sedimentation depends on the initial gap h_0', which can be demonstrated by the snapshot of particle positions shown in Fig. 5 and Fig. 6. For $h_0'=0.5$ Particle 2 (purple) and Particle 3 (dark blue) tend to cluster and form a pair with Particle 2 leading and Particle 3 trailing. Accordingly, as a result of flow symmetry Particle 6

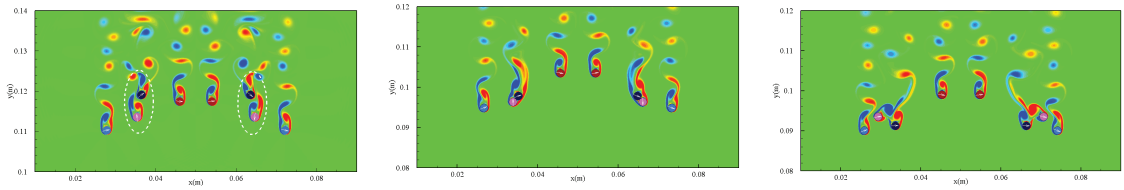

(a) $t'=41.35$ (b) $t'=49.10$ (c) $t'=51.68$

Figure 5: Instantaneous vorticity contour for $h_0'=0.5$.

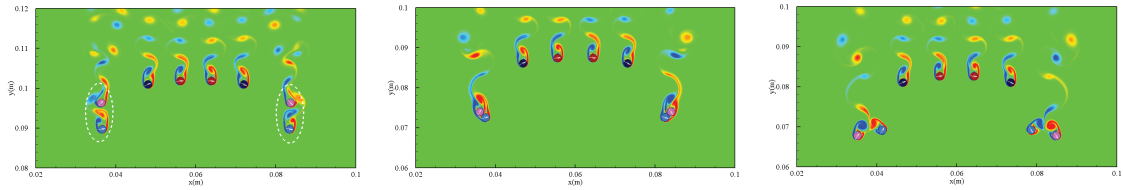

(a) $t'=49.10$ (b) $t'=56.86$ (c) $t'=59.44$

Figure 6: Instantaneous vorticity contour for $h_0'=1.0$.

and Particle 7 also display the similar feature which is shown in Fig. 5. If increasing the initial gap, such as $h_0'=1.0$, the first DKT motion then shifts to the two outermost particles (Particle 1 and Particle 2, Particle 7 and Particle 8) with the light blue particle (Particle 1 and Particle 8) leading and the purple one (Particle 2 and Particle 7) trailing, as shown in Fig. 6. This is consistent with the observation made by Yacoubi et al. (2012). Moreover, it has been shown from Figs. 4-6 that regardless of the value of h_0', the particles display a left and right mirror symmetry in the vortex shedding pattern and correspondingly, a mirror symmetry in the particle rotation. In other words, two particles symmetric about the centreline rotate in opposite directions and shed counter-rotating vortices.

In order to deeply understand the effects of the initial gap on the DKT motion, several simulations have been carried out by varying the initial gap. The dependence of the first DKT motion on h_0' are summarized in Fig. 7, which shows totally three states of the first DKT motion. As the initial gap increases, the first DKT motion takes place shifting from the inside particles to the outside particles, as shown in Fig. 7. The black arrows on each particle are used to visually identify their relative positions when they are drifting in the sedimentation.

Fig. 8 shows trajectories of the settling particles for the initial gap ranging from $h_0'=0.7\sim5.0$. As the particles settle, the array spreads out due to repulsive interactions mediated by the fluid. The effects of the initial gap on the falling patterns are quite clear. When the initial spacing is small such as $h_0'=0.7$, as shown in Fig. 8(a), the falling shape of the array is concave-down and no collisions occur. However, if the simulations continue the DKT motion would take place for the two outermost particles, which has not been observed in the present computational domain. As the initial gap increases, the

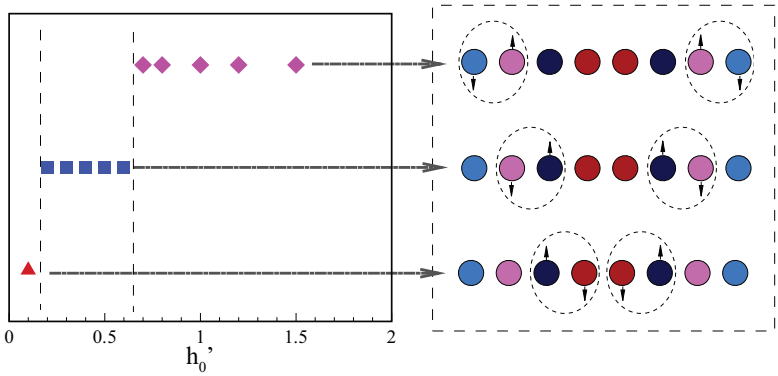

Figure 7: Dependence of the first DKT motion on the initial gap h_0'.

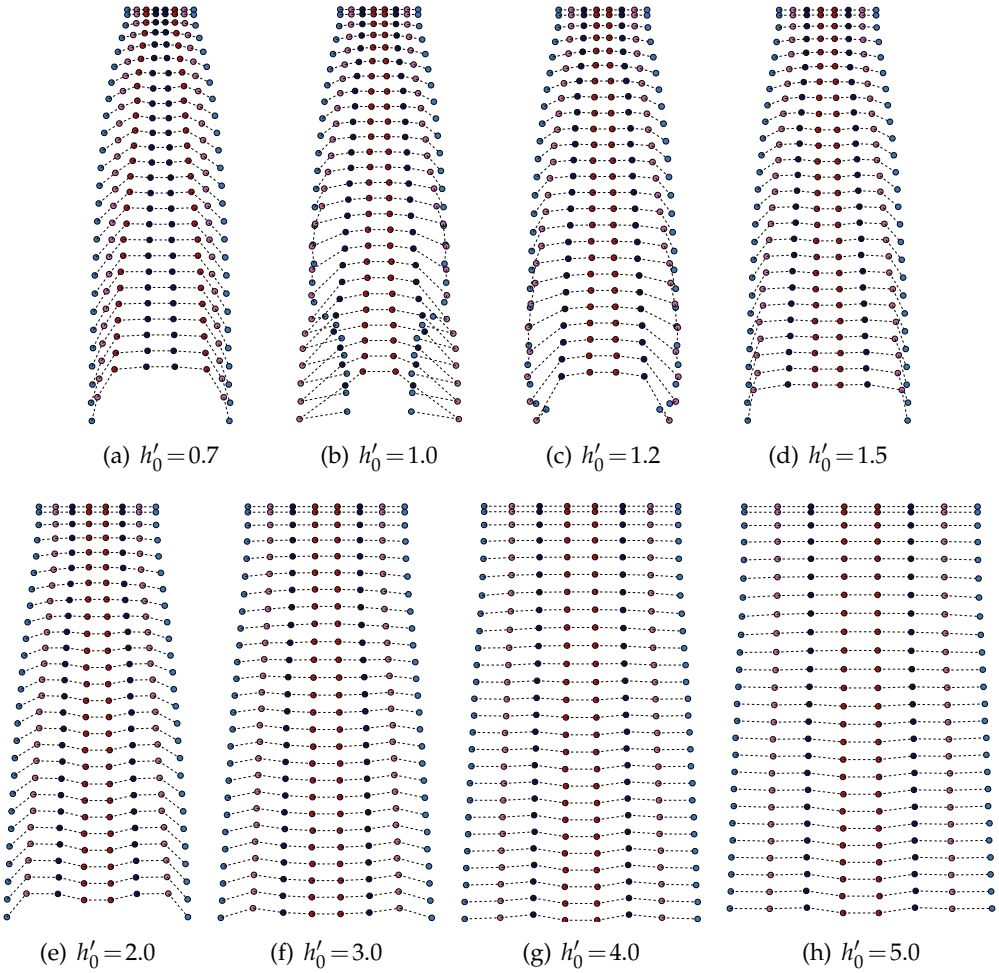

(a) $h_0'=0.7$ (b) $h_0'=1.0$ (c) $h_0'=1.2$ (d) $h_0'=1.5$

(e) $h_0'=2.0$ (f) $h_0'=3.0$ (g) $h_0'=4.0$ (h) $h_0'=5.0$

Figure 8: Trajectories of the particles for different initial gap $h_0'=1.0$.

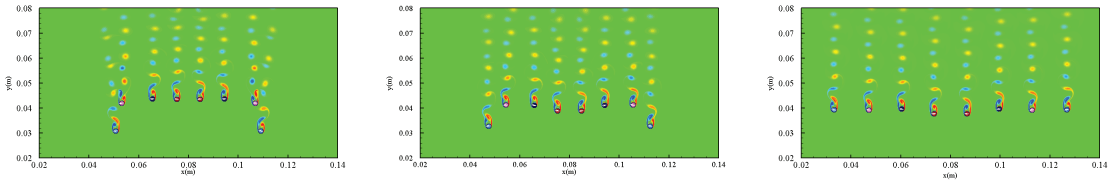

(a) $h_0'=1.5$ (b) $h_0'=2.0$ (c) $h_0'=5.0$

Figure 9: Instantaneous vorticity contour for different initial gaps.

settling particles still display the concave-down falling shape for h_0' up to 1.5, which is broken down by the first DKT motion for $h_0'=1.0$ and $h_0'=1.2$, as shown in Fig. 8(b) and Fig. 8(c). Moreover, the falling shape of $h_0'=1.5$ is different from that of $h_0'=0.7$. There are four particles in the middle of the array which are falling nearly in line for $h_0'=0.7$, however, there are six particles nearly in line for $h_0'=1.5$. As the initial gap is further increasing, the concave-down shape of the array cannot be observed any more. The particles are shaped like the letter "M" when they reach a steady state, as shown in Fig. 8(e) and Fig. 8(f). In these cases the outermost (light blue) particles are always leading. Importantly, the DKT motion is not so easily expected to happen for the "M" falling shape, unlike the concave-down shape. However, the shape of letter "M" is not so apparent when the initial gap is further increasing, such as $h_0'=4.0$ and 5.0, as shown in Fig. 8(g) and Fig. 8(h). All particles are falling nearly in a horizontal line, which suggests that all particles are sedimenting at a similar speed. Therefore, in most cases of an initial horizontal arrangement the final configuration of the particles deviates significantly from the horizontal, which agree with the conclusion made by Yacoubi et al. (2012). Nevertheless, if the initial particle-particle gap is large enough, the final configuration is approaching to the horizontal, which is denoted by "in-line" shape.

Fig. 9 shows the instantaneous vorticity contour of the falling particles with initial gap $h_0'=1.5$, 2.0 and 5.0 at $t'=77.53$, respectively. In all results shown in Fig. 9 the left and right particles rotate in opposite directions and their wakes are symmetric about the centerline. For the result of $h_0'=1.5$, the outermost (light blue) particles are always leading before collisions happen. In the case of $h_0'=2.0$, which shows the falling shape of letter "M", the outermost particles are leading as well. However, the result of $h_0'=5.0$ is different. The two (red) particles in the middle lead instead of the outermost ones.

3.3 Lateral and vertical expansion

Regardless of the value of h_0', it's noticeable that the particles always spread out as they settle. As shown in Fig. 8, the spread of the array is strongly depending on the initial gap. In order to quantitatively understand it, the variance $<X^2(t')>$ is introduced to describe

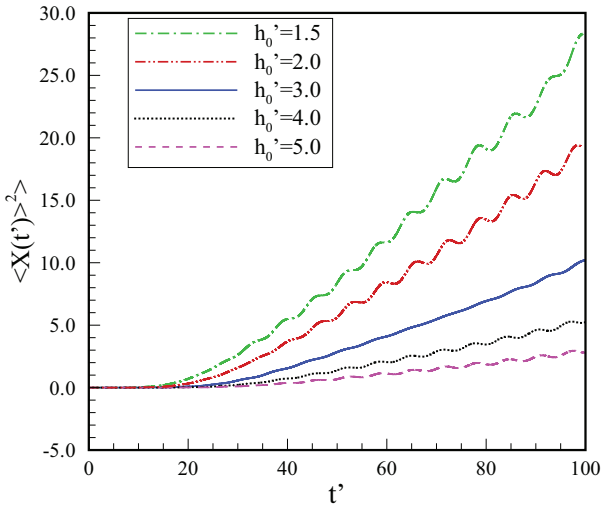

Figure 10: Temporal evolution of the lateral variance of the array.

the lateral expansion of the array in this work, which is defined by,

$$\langle X^2(t')\rangle = \frac{\sum_{k=1}^{n}[x_k(t')-x_k(0)]^2}{nD^2}, \tag{3.1}$$

where n is the number of the particles, x_k is the horizontal position of the kth particle and $t'=t/T$. Fig. 10 shows the temporal evolution the lateral variance of the array for initial gap h_0' ranging from 1.5 to 5.0, which is relatively large so that the particle-particle collisions do not happen. Obviously, the lateral variances of the array are increasing in a nonlinear fashion all the time because of repulsive interaction force mediated by the fluid except in the short initial period. In the initial period the array does not spread out for all values of h_0'. This is because the particle-particle interactions are indirectly transported by the fluid inertia which needs some time to transfer among particles. Furthermore, the larger the initial gap is the more time is needed, which is indicated in Fig. 10. After the initial period, the particles expand laterally all the time. It's also noticeable that the lateral variance is steeply increasing for small initial gap, such as $h_0'=1.5$, which is due to the strong interaction force during the early time of sedimentation, as shown in Fig. 10. Furthermore, it's worth mentioning that oscillations are observed after a period of time for all results except that of $h_0'=3.0$. The reason is not clear.

Similarly, the variance $<Y^2(t')>$ describes the vertical expansion of the array in this work, which is defined by,

$$\langle Y^2(t)\rangle = \frac{\sum_{k=1}^{n}[y_k(t)-y_a]^2}{nD^2}, \qquad y_a=\frac{\sum_{k=1}^{n}y_k(t)}{n}, \tag{3.2}$$

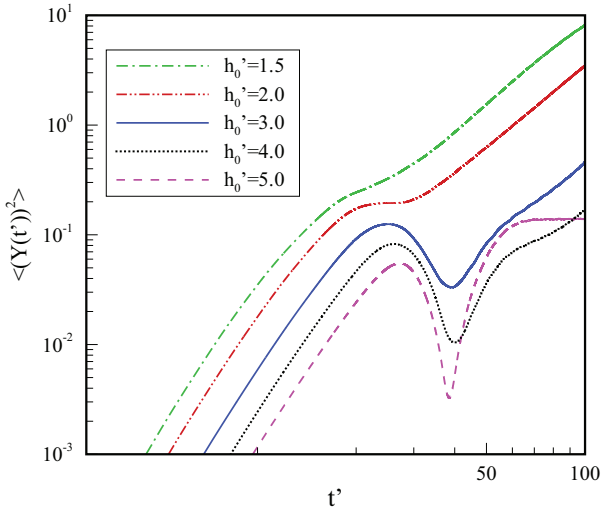

Figure 11: Temporal evolution of the vertical variance of the array.

where y_k is the vertical position of the kth particle. Fig. 11 shows the temporal evolution of the vertical variance of the array. For better visualization of comparison, log-log coordinate system is adopted in Fig. 11. The vertical variance is increasing as time evolves for all initial gap at the early stage (approximately $t' < 25$), which is noticeable in Fig. 11. In addition, all the observed results display the similar growth curve at the early stage. Thereafter the variance continues to increase at a lower speed for small initial gaps, such as $h_0' = 1.5$ and 2.0, after going through a transition region. This suggests that the array expands in the vertical orientation for small initial gaps in the simulations. However, in the transition region, for large initial gaps the variance firstly decreases after the early stage, such as $h_0' = 3.0$ and 4.0, which eventually increases after reaching a minimum, as shown in Fig. 11. The decrease in the vertical variance for large initial gaps is due to the transition from the shape of letter "M" to the shape of "in-line". Interestingly, the similar sub-linear growth is observed at long times for the results of $h_0' = 1.5$-4.0, as shown in Fig. 11. Nevertheless, the variance of $h_0' = 5.0$ is different from other results, which is kept as a constant of about 0.14 at long times. This suggests that if the initial particle-particle gap is large enough the particles would not spread out any more in vertical orientation, and display nearly "in-line" shape.

3.4 Hydrodynamic forces

The lateral and vertical hydrodynamic forces on the particles when they are settling are investigated in this section. Fig. 12 shows the temporal evolution of the lateral (C_x) and vertical (C_y) hydrodynamic force coefficients on the outermost particles, i.e. Particle 1 and Particle 8. The initial particle-particle gap is $h_0' = 5.0$. The coefficients are defined as $C_x = F_x/0.5\rho_f U^2 D$ and $C_y = F_y/0.5\rho_f U^2 D$, where F_x and F_y are the lateral and vertical

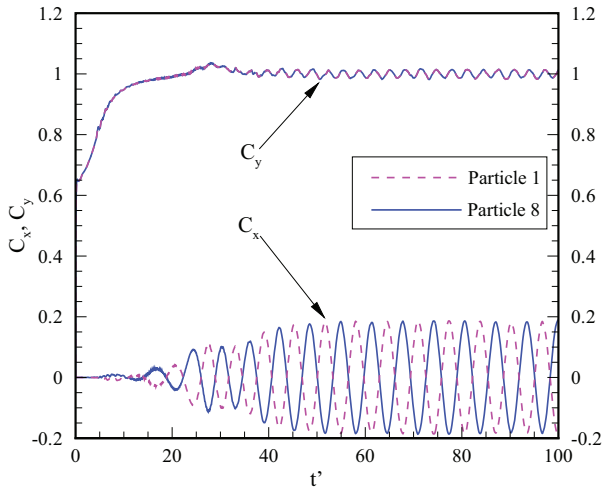

Figure 12: Temporal evolution of lateral (C_x) and vertical (C_y) hydrodynamic force on the selected particles for $h_0'=5.0$.

hydrodynamic force of the particle, respectively. As expected, their hydrodynamic forces are symmetrically bilateral. The vertical force coefficients C_y for both particles are identical. In addition, as shown in the figure, they are periodically oscillating around the value of 1.0 after an initial evolution, which indicates that the vertical hydrodynamic force is balanced by the gravity and buoyancy force. Actually, the velocity scale U defined by Eq. (3.1) is chosen in this manner. In the other hand, the lateral hydrodynamic forces for the two particles are periodically anti-synchronous, as shown in Fig. 12. The maximum value of the lateral force coefficient is about 0.19.

Numerical results show that for the other particles the vertical hydrodynamic forces are similar to that of Particle 1 or Particle 8, thereafter, the lateral hydrodynamic forces are concerned in the following part. Fig. 13 shows the time series of the lateral force coefficients of Particle 1-Particle 4. It's apparent that all the results are displaying similar periodical oscillation after an initial stage of evolution. However, the maximum value of C_x for Particle 1 is a little bigger than the other results. To gain more insight into the lateral hydrodynamic forces of the particles, the power spectrums for the lateral force coefficients of Particle 1 and Particle 4 are shown in Fig. 14, both of which indicate a single frequency, confirming the sinusoidal nature of the lateral force signal for both particles. The value of Strouhal number ($St_p = fD/U$, where f is the primary frequency) in this case is about 0.157, which is smaller than those of flow past fixed cylinder at $Re=100$ or Re=200 as shown in Table 2. Furthermore, numerical results have shown that the value of Strouhal number is the same for all the particles (other results are not shown), indicating that all the particles are oscillating in a similar manner during the sedimentation for $h_0'=$ 5.0.

The effect of initial gap h_0 is also studied. Fig. 15 shows the temporal evolution of

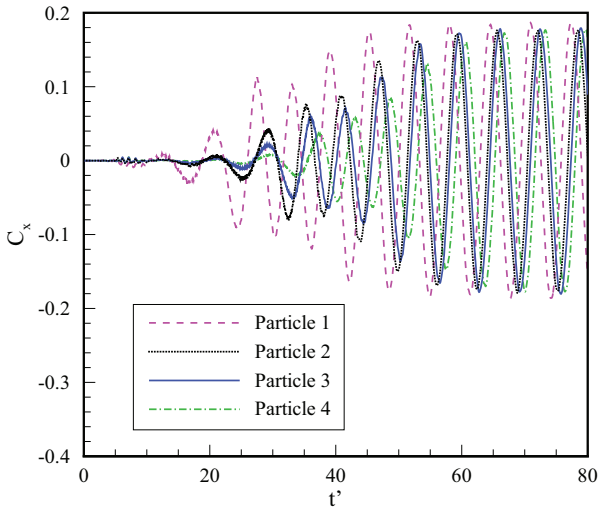

Figure 13: Temporal evolution of lateral hydrodynamic force on the selected particles for $h_0'=5.0$.

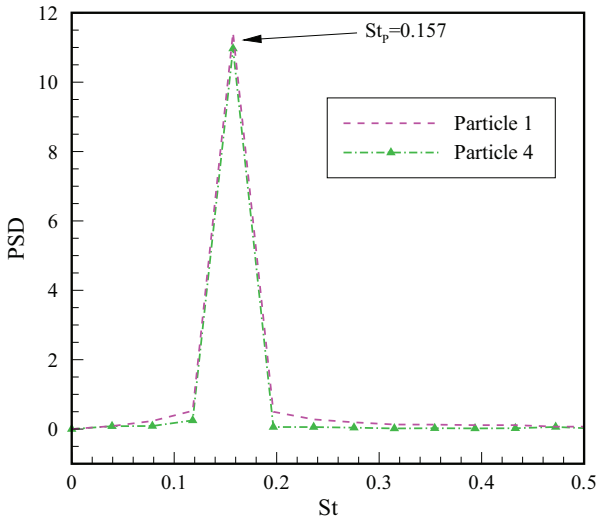

Figure 14: Power spectra of the selected particles for $h_0'=5.0$.

lateral force coefficients of the far left particle (Particle 1) for $h_0'=2$, 3 and 5. The maximum value of lateral force coefficient for $h_0'=3$ is similar to that of $h_0'=5$, which is a little larger than that of $h_0'=2$, as shown in the figure. The power spectrums of these three lateral force coefficients are also shown in Fig. 16. The value of Strouhal number is the same for all cases.

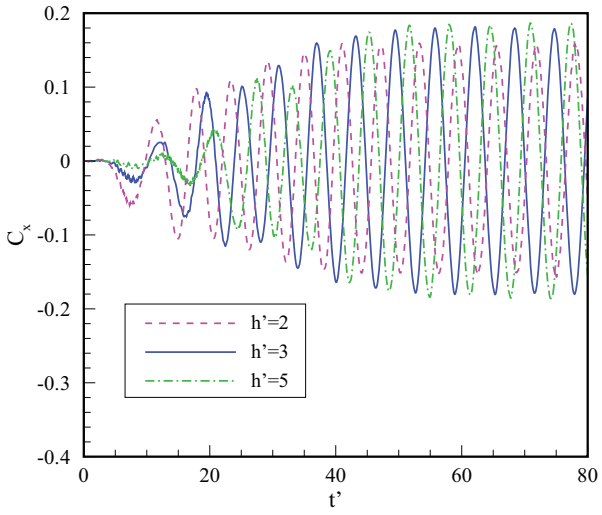

Figure 15: Temporal evolution of lateral hydrodynamic force on the far left particle (Particle 1) for different h_0'.

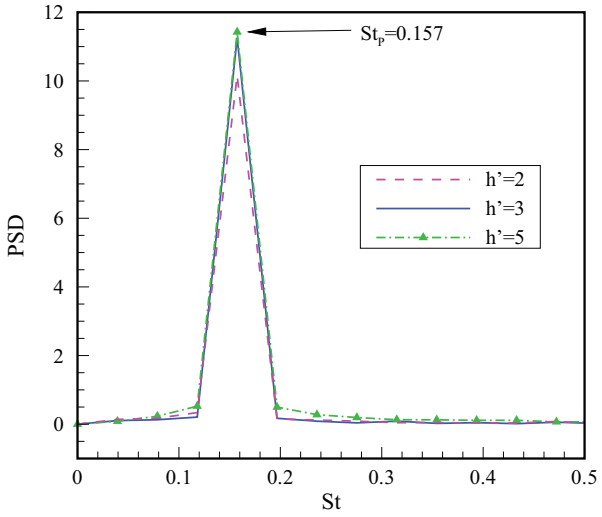

Figure 16: Power spectra of the far left particle for different h_0'.

3.5 Wall effects

In this section the effects of the walls, i.e. the width of the container, on the expansions of the array and falling patterns are examined. Fig. 17 and Fig. 18 shows the temporal evolution of the lateral and vertical variance for $h_0' = 5.0$, respectively. Both of the results of $L_x' = 80$ and $L_x' = 90$ are presented. The effects of the container width are obvious. It's expected that the lateral expansion is dependent on the container width, which is

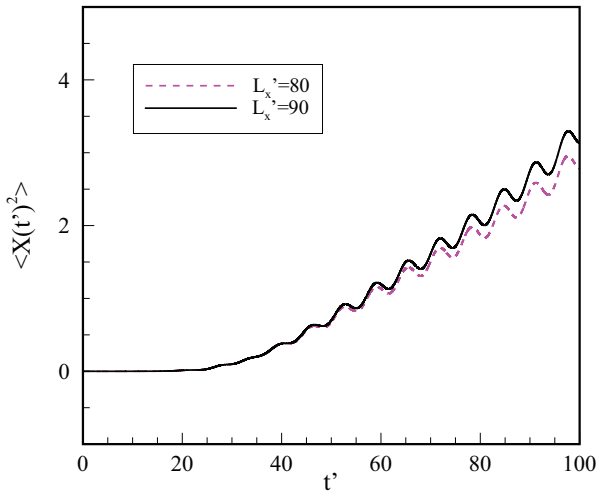

Figure 17: Effects of the container width on the lateral variance of the array for $h_0'=5.0$.

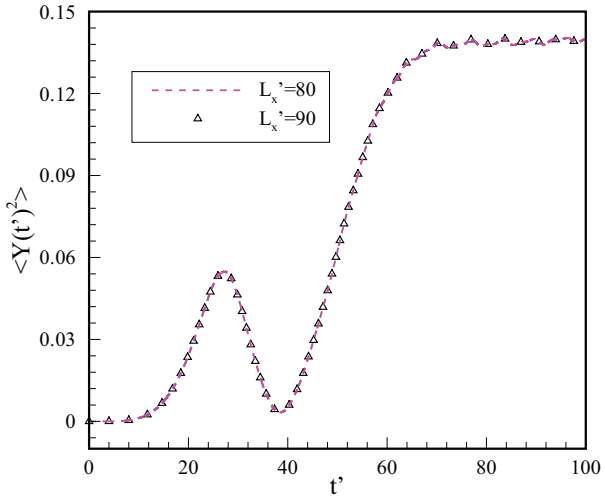

Figure 18: Effects of the container width on the vertical variance of the array for $h_0'=5.0$.

larger to maintain more tendency for the particles to expand laterally, as shown in Fig. 17. However, for the vertical expansion the result of $L_x'=80$ is almost the same as the result of $L_x'=90$, which states that the effects of the container width on the vertical expansion is negligible.

Fig. 19 shows the trajectories of the falling particles for $h_0'=0.7$, 1.5 and 5.0. For each case two kinds of container width are taken into consideration. The corresponding results are shown in the left side and right side of each figure, respectively. The effects of the container width on falling patterns are insignificant, as shown in Fig. 19. The

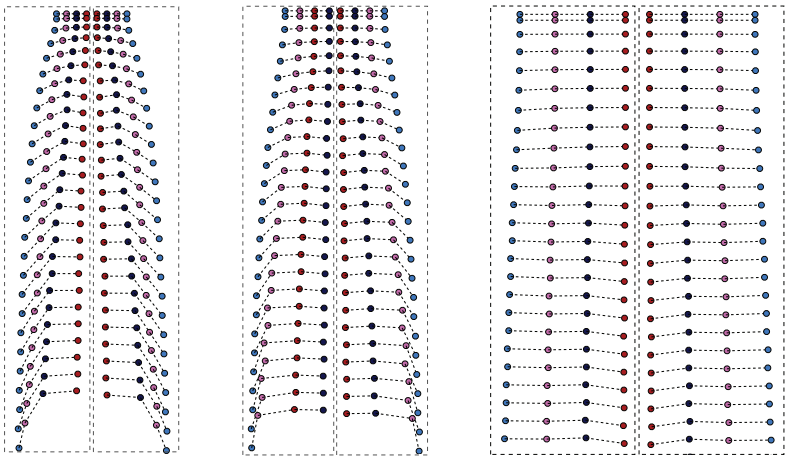

(a) $h_0'=0.7$ (b) $h_0'=1.5$ (c) $h_0'=5.0$

Figure 19: Falling patterns for different container width: (a) $L_x'=50$ (left) and $L_x'=60$ (right) (b) $L_x'=64$ (left) and $L_x'=80$ (right) (c) $L_x'=80$ (left) and $L_x'=90$ (right).

general feature of left side and right side is the same though fine distinction is observed, suggesting that the present computational domains are reasonable for numerical study of falling patterns.

4 Conclusion remarks

In this work the previously developed LB-DF/FD method is updated by replacing the SRT model with the MRT model. The MRT based method is superior to the previous method in computing pressure. Then the method is used to numerically investigate eight circular particles settling under gravity in a container.

Results have shown that the DKT motion may take place several times when the particles are falling. First of all, close attention has been paid to the DKT motion which takes place for the first time because the subsequent DKT motion could be dependent on the repulsive force which is determined through a hypothetical collision model in the simulations. It has been shown that the first DKT motion depends on the initial particle-particle gap, which shifts from the inside particles to the outside particles as initial gap increases.

In addition, the trajectories of the particles, i.e. falling patterns, are studied in detail. The effect of initial gap on the falling pattern is significant. Totally speaking, three kinds of falling patterns are shown when the particle-particle initial gap varies. The concave-down shape of the array is observed when the initial gap is small, while this shape is broken down when the DKT motion takes place. As the initial gap increases the concave-down shape develops to the shape of letter "M", with the outermost particles leading.

In this case the DKT motion is not observed in the simulations. Furthermore, the array is almost in-line when the initial gap is further increasing, and the two particles in the middlemost are leading, instead.

The lateral and vertical expansions of the array, which are expressed by their own variances, are also studied in this work. The lateral variance increases as time evolves, which is larger for smaller initial gap due to stronger repulsive interactions. It is more complex for the vertical variance, which displays the similar growth curve for all initial gaps at the early stage. Thereafter, there exists a transition region for each case, after which all results continue to increase at a similar lower speed except the result of the largest initial particle-particle gap that was simulated, i.e. $h_0'=5.0$. The vertical variance of $h_0'=5.0$ is kept as a constant, instead. This states that the array is shaped like a horizontal line which is expanding laterally when the particles are falling.

The hydrodynamic forces on the particles are studied by introducing their lateral and vertical force coefficients. The results for large initial gap, i.e. $h_0' \geq 2.0$, are taken into account. On one hand, the vertical force coefficients are periodically oscillating with an average value of 1.0 at long times for all particles, indicating that for each particle the vertical hydrodynamic force is balanced by the gravity and buoyant force. On the other hand, the lateral force coefficients are periodically oscillating in a sinusoidal form at long times. The oscillation frequency of lateral force coefficients is the same for all particles and the Strouhal number is about 0.157. Furthermore, there's no significant difference among the amplitudes of lateral force coefficients. The effect of initial gap on the oscillation frequency is negligible.

Finally, the wall effects are examined. The lateral expansion is dependent on the container width, but the vertical expansion is opposite. Importantly, the wall effects on the trajectories of the particles are insignificant, which suggests that this work presents universal features of falling patterns in the present configurations.

Acknowledgments

This work is supported by the Major Program of the National Natural Science Foundation of China (No. 11132008). This work is also supported by Project Nos. 11272302 and 11072229 from the National Natural Science Foundation of China.

References

[1] Aidun, C. K., Lu, Y., Ding, E., 1998. Direct analysis of particulate suspensions with inertia using the discrete Boltzmann equation. J. Fluid Mech. 373, 287-311.
[2] Alexander, M. L., Olga, M. L., Avinoam, N., 2003. The weakly inertial settling of particles in a viscous fluid. Proc. R. Soc. Lond. A 459, 3079-3098.
[3] Brady, J. F., Bossis, G., 1988. Stokesian dynamics. Annu. Rev. Fluid Mech. 20, 111-157.
[4] Braza, M., Chassaing, P., Minh, H. H., 1986. Numerical study and physical analysis of the pressure and velocity fields in the near wake of a circular cylinder. J. Fluid Mech. 163, 79-130.

[5] Crowley, J. M., 1971. Viscosity induced instability of a one-dimensional lattice of falling spheres. J. Fluid Mech. 45, 151-159.
[6] Ding, H., Shu, C., Yeo, K. S., Xu, D., 2007. Numerical simulation of flows around two circular cylinders by mesh-free least square-based finite difference methods. Int. J. Numer. Methods Fluids 53, 305-332.
[7] Feng, J., Joseph, D. D., 1995. The unsteady motion of solid bodies in creeping flows. J. Fluid Mech. 303, 83-102.
[8] Feng, Z. G., Michaelides, E. E., 2004. The immersed boundary-lattice Boltzmann method for solving fluid-particles interaction problems, J. Comput. Phys. 195, 602-628.
[9] Guo, Z. L., Zheng, C. G., Shi, B. C., 2002. Discrete lattice effects on the forcing term in the lattice Boltzmann method. Phys. Rev. E 65, 046308.
[10] Hocking, L. M., 1964. The behaviour of clusters of spheres falling in a viscous fluid. J. Fluid Mech. 20, 365-400.
[11] Jenny, M., Dušek, J., Bouchet, G., 2004. Instabilities and transition of a sphere falling or ascending freely in a Newtonian fluid. J. Fluid Mech. 508, 201-239.
[12] Koch, D. L., Subramanian, G., 2011. Collective hydrodynamics of swimming microorganisms: Living fluids. Annu. Rev. Fluid Mech. 43, 637-659.
[13] Ladd, A. J. C., 1994. Numerical simulations of particulate suspensions via a discretized Boltzmann equation Part I. Theoretical foundation. J. Fluid Mech. 271, 285-310.
[14] Leichtberg, S., Weinbaum, S., Pfeffer, R., Gluckman, M. J., 1976. A study of unsteady forces at low Reynolds number: A strong interaction theory for the coaxial settling of three or more spheres. Phil. Trans. R. Soc. Lond. A 282, 585-610.
[15] Luo, L.-S., Liao, W., Chen, X.W., Peng, Y., Zhang, W., 2011. Numerics of the lattice Boltzmann method: Effects of collision models on the lattice Boltzmann simulations. Phys. Rev. E 83, 056710.
[16] Mark, N. L., Hermann, F. F., 2005. A high-order immersed interface method for simulating unsteady incompressible flows on irregular domains. J. Comput. Phys. 204, 157-192.
[17] Metzger, B., Nicolas, M., Guazzelli, É., 2007. Falling clouds of particles in viscous fluids. J. Fluid Mech. 580, 283-301.
[18] Mo, G., Sangani, A. S., 1994. A method for computing Stokes flow interactions among spherical objects and its application to suspensions of drops and porous materials. Phys. Fluids 6, 1637-1652.
[19] Nguyen, N-Q, Ladd, A.J.C., 2005. Sedimentation of hard-sphere suspensions at low Reynolds number. J. Fluid Mech. 525, 73-104.
[20] Nie, D. M., Lin, J. Z., 2010. A LB-DF/FD method for particle suspensions. Commun. Comput. Phys. 7, 544-563.
[21] Nie, D. M., Lin, J. Z., 2011a. A lattice Boltzmann-direct forcing/fictitious domain model for brownian particles in fluctuating fluids. Commun. Comput. Phys. 9, 959-973
[22] Nie, D., Lin, J., 2011b. Dynamics of two elliptical particles sedimentation in a vertical channel: Chaotic state. Int. J. Comput. Fluid Dyn. 25, 401-406.
[23] Nie, D., Lin, J., Qiu, L., 2013. Direct numerical simulations of the decaying turbulence in rotating flows via the MRT-lattice Boltzmann method. Int. J. Comput. Fluid Dyn. DOI:10.1080/10618562.2013.779679.
[24] Nie, D. M., Wang, Y., Zhang, K., 2011. Long-time decay of the translational/rotational velocity autocorrelation function for colloidal particles in two dimensions. Comput. Math. Appl. 61, 2152-2157.
[25] Nie, D., Lin, J., Zhang, K., 2012. Flow patterns in the sedimentation of a capsule-shaped

particle. Chin. Phys. Lett. 29, 084703.
[26] Qian, Y. H., d'Humieres, D., Lallemand, P., 1992. Lattice BGK models for Navier-Stokes equation. Europhys. Lett. 17, 479-484.
[27] Tian, F. B., Luo, H., Zhu, L., Liao, J. C., Lu, X. Y., 2011. An efficient immersed boundary-lattice Boltzmann method for the hydrodynamic interaction of elastic filaments. J. Comput. Phys. 230, 7266-7283.
[28] Uhlmann, M., 2005. An immersed boundary method with direct forcing for the simulation of particulate flows. J. Comput. Phys. 209, 448-476.
[29] Wan, D., Turek, S., 2007. An efficient multigrid-FEM method for the simulation of solid-liquid two phase flows. J. Comput. Appl. Math. 203, 561-580.
[30] Xu, S., 2008. The immersed interface method for simulating prescribed motion of rigid objects in an incompressible viscous flow. J. Comput. Phys. 227, 5045-5071.
[31] Xu, S., Wang, Z. J., 2006. An immersed interface method for simulating the interaction of a fluid with moving boundaries. J. Comput. Phys. 216, 454-493.
[32] Yacoubi, A. E., Xu, S., Wang, Z. J., 2012. Computational study of the interaction of freely moving particles at intermediate Reynolds numbers. J. Fluid Mech. 705, 134-148.
[33] Yu, Z. S., Shao, X. M., 2007. A direct-forcing fictitious domain method for particulate flows. J. Comput. Phys. 227, 292-314.